Nano Research Energy

ISSN 2791-0091 (print); 2790-8119 (online)
https://doi.org/10.26599/NRE.2026.9120246

Research Article

Ionic layer epitaxy synthesis of ultrathin two-dimensional high-entropy alloy electrocatalyst for highly efficient and stable oxygen evolution reaction

Guangyuan Yan[1] (✉), Tianlu Wang[1], Yuanye Wang[1], Yunhe Zhao[2] (✉), Junwen Zhang[1], and Wenbo Yu[1] (✉)

[1] *School of Mechanical, Electronic and Control Engineering, Beijing Jiaotong University, Beijing 100044, China*
[2] *College of Chemistry, Chemical Engineering and Resource Utilization, Northeast Forestry University, 26 Hexing Road, Harbin 150040, China*

Received: 6 April 2026 / **Revised:** 22 June 2026 / **Accepted:** 27 June 2026 / **Published date:** 16 July 2026

ABSTRACT

Confined to ultrathin two-dimensional (2D) architectures, high-entropy alloys (HEAs) could leverage synergistic cocktail effects and entropy-stabilized phases to enable exceptional oxygen evolution reaction (OER) kinetics and stability via maximized specific surface areas and quantum confinement. However, synthesizing atomically precise 2D HEAs remains fundamentally challenging due to disparate metal nucleation kinetics. Herein, we demonstrate a facile low-temperature (80 °C) ionic layer epitaxy synthesis of ultrathin 2D HEA FeCoNiMo. The OER catalytic activity exhibited a strong inverse correlation with the 2D HEA thickness, where atomic-scale dimensional reduction significantly enhanced electrocatalytic performance. Atomic-scale confinement to 1.1 nm thickness unlocks exceptional OER performance. This 1.1 nm 2D HEA FeCoNiMo revealed a record-low overpotential of 79 mV at 10 mA·cm^{-2} and unprecedented stability (<10% activity decay after 1532 h operation). Especially, its benchmark mass activity (9725.2 A·g^{-1}) represented three orders of magnitude enhancement over IrO_2 (5.7 A·g^{-1}) at the same overpotential of 79 mV. Density functional theory (DFT) reveals that thickness reduction facilitates charge redistribution toward Fe active sites, optimizes the rate-determining step energy barrier, and strengthens adsorbate-catalyst interactions. This work provides fundamental insights into 2D confinement effects in HEAs and establishes a general strategy for designing highly efficient electrocatalysts for sustainable energy applications.

KEYWORDS

high-entropy alloy, two-dimensional nanomaterials, ionic layer epitaxy, oxygen evolution reaction, electrocatalysis

1 Introduction

The oxygen evolution reaction (OER), a critical half-reaction for sustainable energy technologies such as water electrolysis and metal-air batteries, is severely hindered by its intrinsically sluggish kinetics, high overpotential, and insufficient long-term stability of electrocatalysts [1–4]. Traditional noble metal-based electrocatalysts (e.g., RuO_2, IrO_2) suffer from prohibitive costs and scarcity, driving research toward non-precious alternatives [5–7]. High-entropy alloys (HEAs), characterized by their multi-principal elemental compositions and entropy-driven phase stability, have emerged as a promising class of OER electrocatalysts due to their tunable electronic structures, exceptional corrosion resistance, and synergistic "cocktail effects" [8–15]. Among the diverse compositional systems of HEAs, the quaternary FeCoNiMo HEA composed of non-noble metallic elements (Fe, Co, Ni, and Mo) has demonstrated considerable potential in electrocatalytic applications. This promising performance originates from two critical factors: (i) the exceptional structural compatibility between Mo and the 3d transition metals (Fe, Co, Ni), and (ii) the distinctive electronic configuration of Mo's 4d orbital characterized by partial filling states and robust electron-donating capability, which drives strong orbital hybridization between Mo 4d and 3d orbitals of adjacent Fe/Co/Ni atoms [16–18]. However, conventional bulk or nanoparticle HEA often suffer from limited active site exposure, inefficient mass/charge transfer, and morphological homogeneity, which restrict their catalytic activity and practical scalability [9, 19]. These challenges underscore the urgent need to engineer HEAs electrocatalysts with optimized morphologies to unlock their intrinsic catalytic potential.

The design of ultrathin two-dimensional (2D) HEAs nanostructures represents a transformative strategy to address the limitations of bulk and nanoparticle counterparts. Ultrathin 2D materials with a thickness of only one or a few atomic layers (less than 5 nm), inherently offer ultrahigh surface-to-volume ratios, fully exposed active sites, and rapid electron transport pathways, which are critical for enhancing OER kinetics [20–32]. Moreover,

Address correspondence to Guangyuan Yan, gyyan@bjtu.edu.cn; Yunhe Zhao, zhaoyunhe@nefu.edu.cn; Wenbo Yu, wbyu@bjtu.edu.cn

the atomic-level thickness of 2D HEAs enables pronounced lattice distortions and entropy-stabilized interfaces, synergistically optimizing adsorption energetics for reaction intermediates [23, 24]. Despite their promise, the controlled synthesis of 2D HEAs with atomic-level thickness and well-defined interfaces remains challenging owing to the distinct nucleation/growth kinetics of varied compositional metals in HEAs. Traditional methods, such as mechanical exfoliation or chemical vapor deposition (CVD), often yield irregular morphologies, non-uniform elemental distributions, or phase segregation, particularly for alloys with five or more components [24]. The existing novel synthesis methods of two-dimensional high-entropy nanomaterials often require complex protocols and high synthesis temperature (generally higher than 500 °C) or suffer from structural instability during electrocatalysis [19, 24–26]. Thus, developing simple, robust and scalable synthesis routes capable of atomic-level thickness control and elemental homogeneity is critical for advancing 2D HEAs electrocatalysts.

A simple solution-based ion-layer epitaxy (ILE) method is promising to be an innovative solution to overcome these synthesis barriers. ILE leverages self-assembled surfactants at water-air interface as templates to guide the growth of ultrathin two-dimensional structures [27]. The ILE method fundamentally circumvents the symmetry constraints of crystals growth and induces pronounced anisotropic growth dynamics [27, 28]. This mechanism significantly suppresses vertical stacking while markedly promoting lateral expansion of crystals, thus enabling the nucleation and epitaxial growth of ultrathin 2D architectures with atomic-scale thickness [28, 29]. Crucially, this approach operates under exceptionally mild thermal conditions (ambient to 90 °C), requiring neither complex instrumentation nor energy-intensive processes. Its paramount advantages reside in the precise control over both thickness and crystal structure, achieving single-unit-cell thickness uniformity and synthesizing large-area single-crystalline domains [23, 30, 31].

Herein, we demonstrate the rational design of ultrathin 2D HEA FeCoNiMo nanostructures via ILE methodology. Remarkably enhanced OER electrocatalytic activity was achieved upon thickness reduction of the 2D HEA FeCoNiMo nanofilm to 1.1 nm. The optimized 1.1-nm 2D HEA FeCoNiMo catalyst demonstrated exceptional catalytic kinetics, exhibiting an ultralow overpotential of 79 mV at 10 mA·cm^{-2}, a reduced Tafel slope of 30.5 mV·dec^{-1}, and minimal charge transfer resistance (8.2 Ω). Particularly noteworthy are its record-breaking mass activity (9725.2 A·g^{-1}) and turnover frequency (1.94 s^{-1}) at an overpotential of 79 mV, enabled by the atomic-scale thickness. This mass activity surpasses that of commercial IrO_2 benchmarks by three orders of magnitude. The ultrathin 2D HEA electrocatalyst further exhibits unprecedented operational durability, maintaining 90% initial activity after 1532 hours of continuous operation under chronoamperometric testing conditions. Density functional theory (DFT) theoretical simulations further reveal that the thickness reduction of ultrathin 2D HEA promoted the charge redistribution of different metal active sites, optimized the energy barrier of OER rate-limiting step (*OOH→O_2), and thereby enhanced the catalytic activity. This work establishes 2D HEA nanostructures as a materials design paradigm for sustainable energy conversion systems.

2 Experimental

2.1 Materials

Molybdic Acid (H_2MoO_4, 99.00%), nickel chloride hexahydrate ($NiCl_2·6H_2O$, 99.00%), cobalt chloride hexahydrate ($CoCl_2·6H_2O$, 99.00%) ferrous chloride tetrahydrate ($FeCl_2·4H_2O$, 99.00%), formaldehyde (CH_2O), stearic acid (SA, 99.00%), oleylamine (OAM, 99.00%), hydrochloric acid (HCl, 0.01 mol·L^{-1}), dichloromethane ($CHCl_2$, 99.50%), sodium hydroxide (KOH, 99.99%) and Iridium oxide (IrO_2, 99.95%) were purchased from Shanghai Titan Scientific Co., Ltd and directly used without any purification. The deionized water with the resistivity of 18.25 MΩ cm was purified with a water ultrapure cation system.

2.2 Synthesis of ultrathin 2D high-entropy alloy FeCoNiMo

The ionic layer epitaxy (ILE) method was employed to synthesize the ultrathin 2D high-entropy alloy (HEA) FeCoNiMo. In a typical process, 10 mL aqueous solution containing 1.5 mM H_2MoO_4, 1.5 mM $NiCl_2$, 1.5 mM $CoCl_2$, 1.5 mM $FeCl_2$ and 1.2 μL of CH_2O, was prepared in a 15 mL glass vial as the precursor solution. The as-prepared precursor solution was then left standing in the air for 20 min. After that, 10 μL dichloromethane solution of mixed surfactants containing (~0.7 vol.%) stearic acid (SA) solution and (~0.3 vol.%) oleylamine (OAM) solution, was spread on the water surface. The SA solution had a concentration of 1.8 mol·L^{-1}. The OAM solution had a concentration of 1.8 mol·L^{-1} and mixed with hydrochloric acid to a concentration of 0.01 mol·L^{-1}. This two-layer solution was exposed in atmosphere for 10 min to allow the dichloromethane to evaporate. Subsequently, the glass vial was capped and carefully transferred in the convection oven at the temperature of 80 °C. The ultrathin 1.1-nm-thick 2D HEA FeCoNiMo were synthesized after the reaction time of 120 min. The as-synthesized 1.1 nm 2D HEA FeCoNiMo at water-air interface were transferred onto the surface of the substrates by directly scooping using the substrates, and then dried naturally in air for further characterization. SiO_2-coated Si substrates were employed for scanning electron microscope (SEM) and AFM characterization. 50 nm thick Au-coated Si substrates and holy carbon grids were used for X-ray photoelectron spectroscopy (XPS) characterization and transmission electron microscopy (TEM) characterization, respectively. The fluorine-doped tin oxide (FTO) glass substrates were used for electrocatalytic OER measurement. For comparison, the control samples of thicker 3.3 nm 2D HEA FeCoNiMo and 4.6 nm 2D HEA FeCoNiMo were also prepared by the same ILE process where the reaction time was increased to 60 °C and 80 °C, respectively.

2.3 Material characterizations

Sample morphology was characterized using a Zeiss EVO 18 field-emission scanning electron microscope. AFM topography mapping was conducted on a Bruker Dimension Icon system. To minimize tip-convolution artifacts, height profiles were extracted exclusively across sharp step edges where vertical dimensions were accurately represented. XPS analysis employed a wltra-DLD XPS instrument. High-angle annular dark-field scanning transmission electron microscopy (HAADF-STEM) and energy-dispersive X-ray spectroscopy (EDS) elemental mapping were performed using a probe Cs-corrected FEI Titan Themis TEM operated at 200 kV. Crystal structure analysis utilized an FEI TF30 transmission electron microscope at 300 kV.

2.4 Electrochemical testing

OER catalytic performance of ultrathin 2D HEA FeCoNiMo and

control samples was evaluated using a CHI660E electrochemical workstation with a standard three-electrode configuration. Measurements employed N_2-saturated 1 M KOH electrolyte (pH 13.6 ± 0.1), with 2D HEA catalyst-coated FTO substrates (geometric area: 0.5 cm^2) serving as working electrodes. A saturated Ag/AgCl reference electrode and platinum foil counter electrode completed the circuit. Polarization curves were acquired at 5 $mV \cdot s^{-1}$ under continuous oxygen evolution. Electrochemical impedance spectroscopy (EIS) measurements spanned 100 kHz to 1 Hz (AC amplitude: 5 mV) at open-circuit potential. The uncompensated resistance (Ru) was determined by EIS at the open-circuit potential, with the high-frequency intercept on the real axis of the Nyquist plot yielding a value of Ru (Table S1 in the Electronic Supplementary Material (ESM)). All polarization curves presented in this work were *iR*-corrected, where *i* represents the measured current. Long-term stability was assessed via chronoamperometry at fixed overpotential. All potentials were referenced to the reversible hydrogen electrode (RHE) scale. TOF was calculated using the equation: $TOF=(j \times A)/(4 \times F \times n)$, where *j* ($mA \cdot cm^{-2}$) is the current density at a given overpotential, A is the working electrode surface area, *F* is the Faraday constant (96,500 $C \cdot mol^{-1}$), and *n* (mol) is the moles number of the active materials. The equation mass activity=j/m was calculated to mass activity, where *m* ($mg \cdot cm^{-2}$) is the mass loading of the working electrode and *j* ($mA \cdot cm^{-2}$) is the measured current density at given potential. For 1.1, 3.3, and 4.6 nm thick 2D HEA samples, the mass loadings per unit geometric area were quantified by a combined DFT-experimental approach: volume = area × thickness, density = DFT-optimized (8.15 $g \cdot cm^{-3}$), yielding 0.90, 2.69, and 3.75 $\mu g \cdot cm^{-2}$, respectively. These values were consistently used for all mass-normalized activity comparisons. All electrochemical measurements, including those for the reference IrO_2 catalyst, were conducted under strictly identical conditions, including the same electrolyte, scan rate, temperature, and electrode configuration. The same mass loading of both 1.1 nm 2D HEA and commercial IrO_2 was precisely controlled.

2.5 DFT calculations

All density functional theory calculations were performed by Vienna *ab initio* simulation package (VASP). The Perdew-Burke-Ernzerhof (PBE) functional was employed to treat the exchange-correlation interactions. The plane-wave basis set with a kinetic energy cutoff of 400 eV, the energy convergence criterion of 10^{-4} eV, the force convergence criterion of 0.05 $eV \cdot Å^{-1}$, and a (2×2×1) Monkhorst-Pack k-point sampling was employed for structure relaxation. A sufficiently large vacuum gap (> 12 Å) was employed to prevent the interaction between neighboring periodic structures. H_2 and H_2O were calculated in boxes of 20 Å×20 Å× 20 Å with the gamma point only. The free energy diagrams for OER were calculated with reference to the computational hydrogen electrode. Spin-polarized calculations were employed throughout our DFT simulations. Given the metallic nature of our 2D HEA, no Hubbard *U* correction was applied, as standard PBE functional adequately describes the delocalized electronic states in transition metal alloys. The free energy of gas phase and adsorbed species can be obtained from the following equation:

$$\Delta G = \Delta E_{DFT} + \Delta ZPE - T\Delta S$$

where ΔE_{DFT} was the electronic energy difference. ΔZPE and $T\Delta S$ was the change in the zero-point energy and entropy.

3 Results and discussion

3.1 Synthesis of ultrathin 2D HEA FeCoNiMo

The ultrathin 2D HEA FeCoNiMo was fabricated via an innovative ILE approach at the water-air interface mediated by a binary surfactants monolayer consisting of stearic acid (SA) and oleylamine (OAM), as schematically illustrated in Fig. 1(a) (complete synthetic protocols were detailed in Experimental details). The aqueous precursor solution comprised an equimolar mixture (1.5 mM each) of H_2MoO_4, $NiCl_2$, $CoCl_2$, $FeCl_2$ and a trace amount of CH_2O, maintained at a weakly acidic pH. Under weakly acidic conditions, SA underwent partial deprotonation to form negatively charged carboxylate headgroups, while OAM was protonated to generate positively charged ammonium headgroups. These complementary surfactants spontaneously self-assembled into a highly ordered mixed monolayer through electrostatic complementarity and hydrophobic interactions. This engineered interface created spatially distinct electrostatic domains: anionic MoO_4^{2-} species were preferentially adsorbed at OAM-rich cationic regions, while divalent transition metal cations (Fe^{2+}, Co^{2+}, Ni^{2+}) accumulated at SA-dominated anionic domains, forming a metastable ionic confinement layer with sub-nanometer thickness. This spatial preorganization effectively reduced the diffusion length to atomic scale, suppressing elemental segregation during nucleation. The subsequent CH_2O-mediated reduction at 80 °C triggered simultaneous nucleation of all four metal species within the confined template, while the high configurational entropy further thermodynamically disfavored phase separation by lowering the Gibbs free energy of the mixed solid solution relative to segregated phases. This synthesis process resulted in the epitaxial growth of crystalline HEA nanostructures within the 2D confined region. Furthermore, this ILE system underscored the critical importance of dual-surfactant strategy, which achieved both spatial confinement and kinetic control, enabling the formation of a uniform single-phase alloy at the atomic scale. While the use of single surfactants or improper reductants led to severe phase segregation and inhomogeneous morphologies in other high-entropy systems [32].

3.2 Morphological and structural characterization

The morphological characteristics of the as-synthesized ultrathin 2D HEA FeCoNiMo were systematically investigated through scanning electron microscopy (SEM). Figure 1(b) presents a representative low-magnification SEM micrograph of 2D HEA nanostructure on a SiO_2-coated Si substrate, revealing a continuous nanofilm architecture with lateral dimensions exceeding 4000 μm. Notably, the nanofilm exhibited a smooth, defect-free surface morphology devoid of observable wrinkles or overlapping features. Higher-resolution SEM examination (inset, Fig. 1(b)) demonstrated homogeneous contrast distribution across the entire specimen, indicative of uniform thickness throughout 2D HEA structure. Complementary AFM topographic analysis (Fig. 1(c)) corroborated the thickness uniformity, revealing an ultrathin profile of approximately 1.1 nm (Fig. 1(d)). Quantitative surface roughness evaluation demonstrated exceptional planarity, with a roughness value of merely 0.05 nm, confirming the atomic-level flatness of the synthesized 2D HEA. Through controlled extension of the ionic layer epitaxy (ILE) reaction duration, we successfully engineered 2D HEA FeCoNiMo nanostructures with larger thickness. As demonstrated in Figs. S1 and S2 in the ESM, these thicker 2D HEA maintained comparable morphological

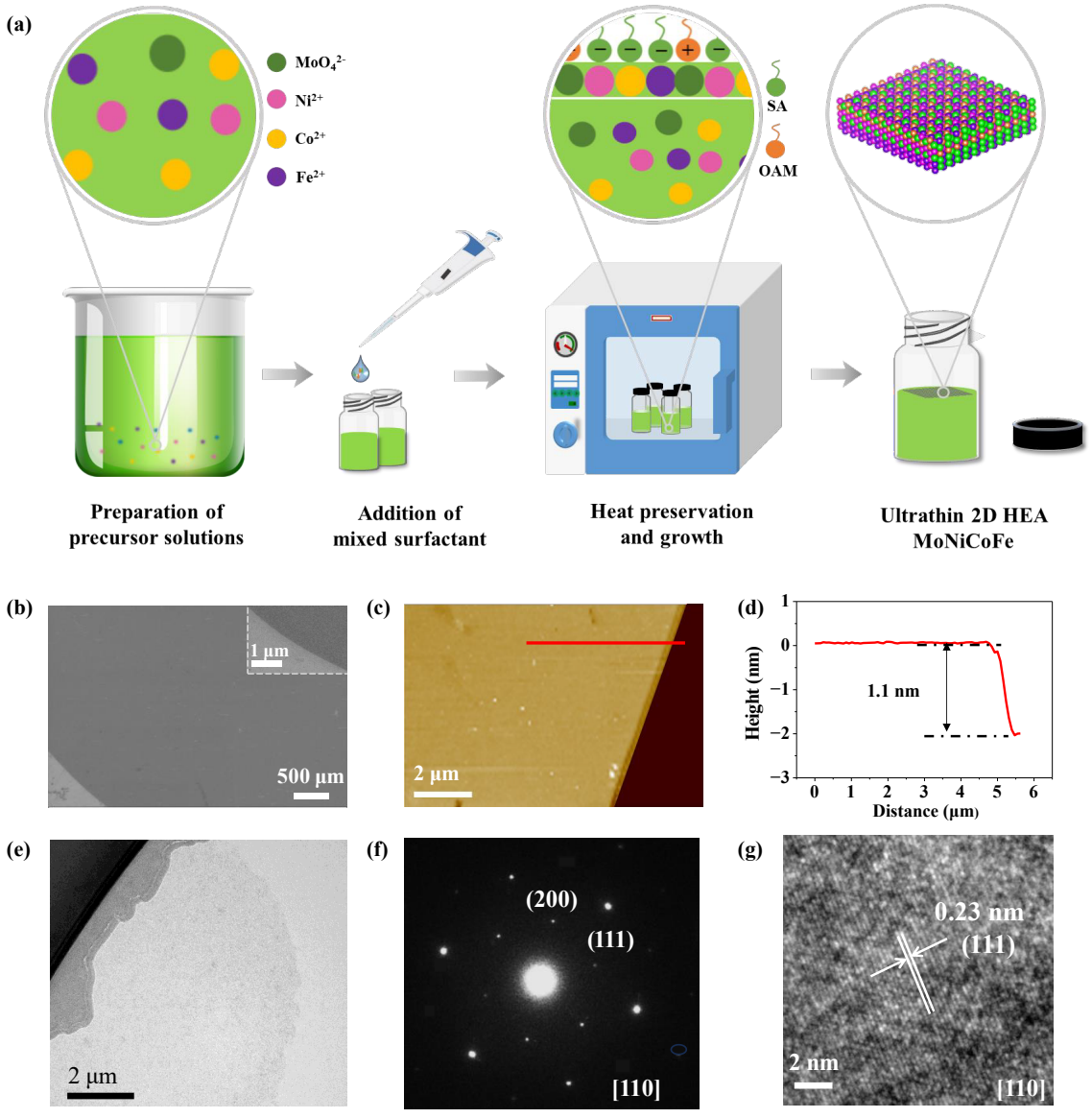

Figure 1 ILE synthesis process, morphological and structural characterization of 1.1-nm-thick ultrathin 2D HEA MoNiCoFe. (a) ILE synthesis process; (b) Low-magnification SEM image, inset is high-magnification SEM image; (c) AFM topography image; (d) Height profile along the red dashed line in corresponding AFM image; (e) Low-magnification TEM image; (f) SAED; (g) HRTEM image.

characteristics of continuous nanofilms while exhibiting progressive thickness increments to 3.3 nm and 4.6 nm, respectively. This thickness tunability highlights the precision of the ILE methodology in fabricating dimensionally controlled 2D HEAs.

The crystal structure of the ultrathin 2D HEA FeCoNiMo was rigorously analyzed via transmission electron microscopy (TEM). Low-magnification TEM imaging (Fig. 1(e)) revealed homogeneous contrast distribution across the entire specimen, corroborating the thickness uniformity previously established by AFM and SEM analyses. Corresponding selected-area electron diffraction (SAED) characterization (Fig. 1(f)) demonstrated a periodic array of sharp diffraction spots, unambiguously confirming the single-crystalline nature of the 2D HEA. Quantitative analysis of the diffraction pattern revealed interplanar spacings corresponding to the (200) and (111) crystallographic planes of a *fcc* solid solution structure aligned along the [110] zone axis [31–34]. High-resolution TEM (HRTEM) image (Fig. 1(g)) resolved atomic-scale lattice fringes with a measured d-spacing of 0.23 nm, corresponding to the (111) planes. This value exhibited close correspondence with both the SAED-derived lattice parameters and theoretical predictions for a rock-salt configuration. The combined structural evidence including SAED symmetry, HRTEM lattice resolution, and interplanar spacing consistency, definitively established that the quaternary Mo-Fe-Co-Ni system adopted a single-phase disordered fcc solid solution structure without detectable secondary phases or compositional segregation. TEM images of 3.3-nm-thick and 4.6-nm-thick ultrathin 2D HEA FeCoNiMo were presented in Figs. S3 and S4 in the ESM, and the results revealed they exhibited same single-crystal rock-salt crystal structure.

3.3 Elemental characterization

XPS was employed to probe the elemental composition and oxidation states of the 1.1-nm-thick ultrathin 2D HEA FeCoNiMo. High-resolution spectra (Figs. 2(a)–2(d)) revealed characteristic signatures of metallic constituents [16]. Fe 2p exhibited principal peaks at 708.8 eV ($2p_{3/2}$) and 722.4 eV ($2p_{1/2}$)

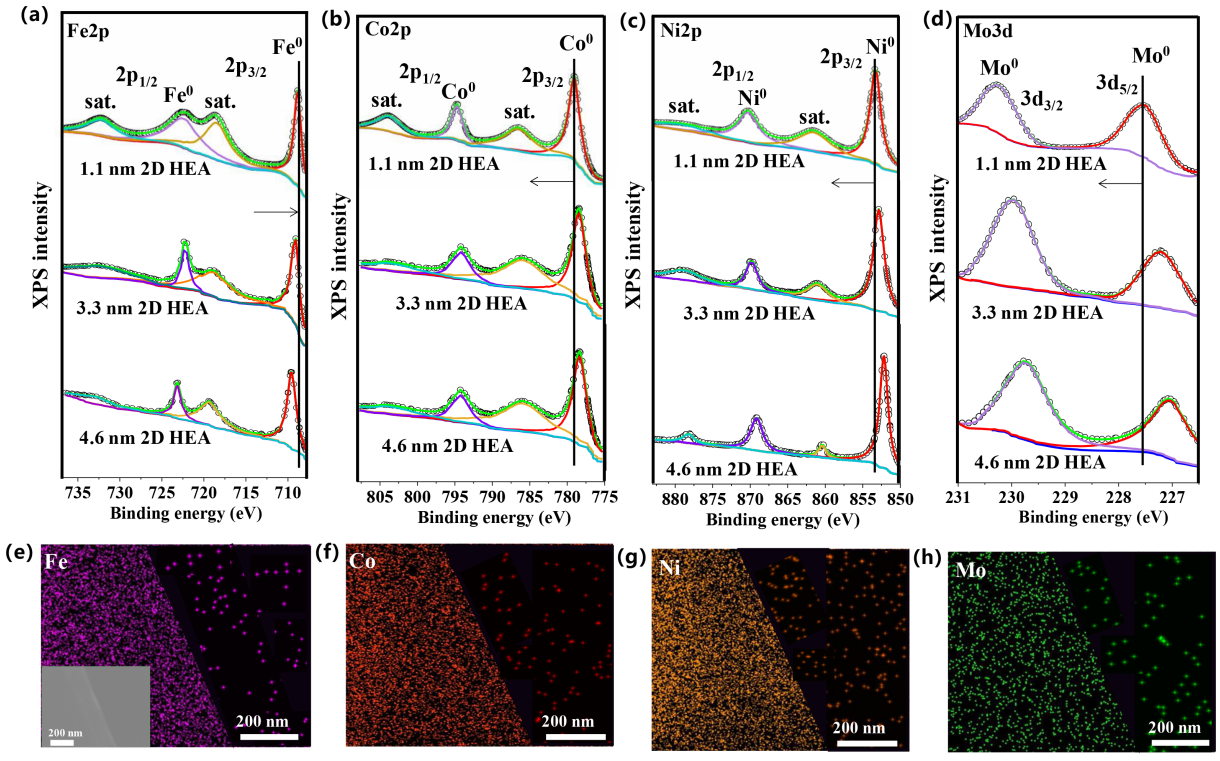

Figure 2 Elemental characterization. (a) Fe 2p XPS spectra, (b) Co 2p XPS spectra, (c) Ni 2p XPS spectra and (d) Mo 3d XPS spectra of 1.1-nm-thick 2D HEA MoNiCoFe, 3.3-nm-thick 2D HEA MoNiCoFe and 4.6-nm-thick 2D HEA MoNiCoFe. STEM-EDX elemental mapping of (e) Fe, (f) Ni, (g) Co and (h) Mo. Inset in (e) is the HAADF-STEM image.

with satellite features at 718.5 eV and 732.3 eV, consistent with Fe^0. Co 2p displayed core-level emissions at 778.9 eV ($2p_{3/2}$) and 794.7 eV ($2p_{1/2}$) accompanied by satellites at 786.4 eV and 803.8 eV, indicative of Co^0. Ni 2p spectra deconvoluted into spin-orbit components at 853.1 eV ($2p_{3/2}$) and 870.1 eV ($2p_{1/2}$) with characteristic satellites, confirming Ni^0. Mo 3d manifested as a doublet at 227.5 eV ($3d_5/_2$) and 230.2 eV ($3d_{3/2}$), corresponding to Mo^0. These analyses collectively verified the predominant metallic character of all constituent elements. Notably, progressive thickness reduction from 4.6 nm to 3.3 nm and 1.1 nm induced systematic binding energy displacements. Fe 2p shifted to lower energies (electron enrichment), while Co 2p, Ni 2p, and Mo 3d migrated to higher energies (electron deficiency). This reciprocal energy shift profile suggests charge transfer from Co/Ni/Mo to Fe atoms, implying synergistic electronic interactions potentially beneficial for OER electrocatalysis. Quantitative XPS analysis (Table 1) established near-equimolar stoichiometry ($Fe_{0.25}Co_{0.24}Ni_{0.25}Mo_{0.26}$) across all thickness variants (1.1–4.6 nm). Spatially resolved STEM-EDS elemental mapping (Figs. 2(e)–2(h), and Figs. S5 and S6 in the ESM) further confirmed homogeneous distribution of all metallic constituents without detectable phase segregation in ultrathin 2D HEA FeCoNiMo. Although the configurational entropy for our equimolar FeCoNiMo system was calculated as 1.39R, the "high-entropy" concept has been widely extended to this four-component equimolar systems that exhibit entropy-stabilized single-phase solid solutions and severe lattice distortion, characteristics that were fully consistent with these observations. To further verify that phase stability was indeed entropy-driven rather than enthalpy-driven, the mixing enthalpy of the FeCoNiMo system was calculated using Miedema's model, yielding a near-zero positive value, suggesting that the phase formation is not governed by strong exothermic interatomic interactions. Furthermore, the single-phase fcc solid solution structure confirmed by SAED, combined with the uniform elemental distribution from EDS mapping, supports entropy-driven phase stabilization.

3.4 Electrocatalytic OER performance

The OER electrocatalytic performance of ultrathin 2D HEA FeCoNiMo on fluorine-doped tin oxide (FTO) substrates was systematically evaluated in 1 M KOH electrolyte. To exclude contributions from the FTO substrate, we performed blank control experiments under identical conditions using bare FTO, which exhibited negligible OER activity (Fig. S7 in the ESM). Linear sweep voltammetry measurements (Fig. 3(a)) revealed that the 1.1 nm 2D HEA delivered exceptional catalytic activity, requiring merely 79 mV overpotential to achieve 10 $mA{\cdot}cm^{-2}$ current density (Fig. S8 in the ESM). Comparative analysis demonstrated a distinct thickness-dependent activity trend. Thicker 2D HEA exhibited higher overpotential of 126 and 237 mV for 3.3 nm and 4.6 nm 2D HEA, respectively. Remarkably, the ultrathin (1.1 nm) HEA outperformed commercial IrO_2

Table 1 Chemical composition of ultrathin 2D HEA FeCoNiMo by XPS quantification analysis

	Fe (wt.%)	Co (wt.%)	Ni (wt.%)	Mo (wt.%)	C (wt.%)	Atom ratio of Fe/Co/Ni/Mo
1.1 nm	4.6	4.7	4.8	8.1	77.8	0.25:0.24:0.25:0.26
3.3 nm	5.9	5.5	5.5	9.5	73.6	0.27:0.24:0.24:0.25
4.6 nm	4.5	4.2	4.6	7.5	79.2	0.26:0.23:0.25:0.26

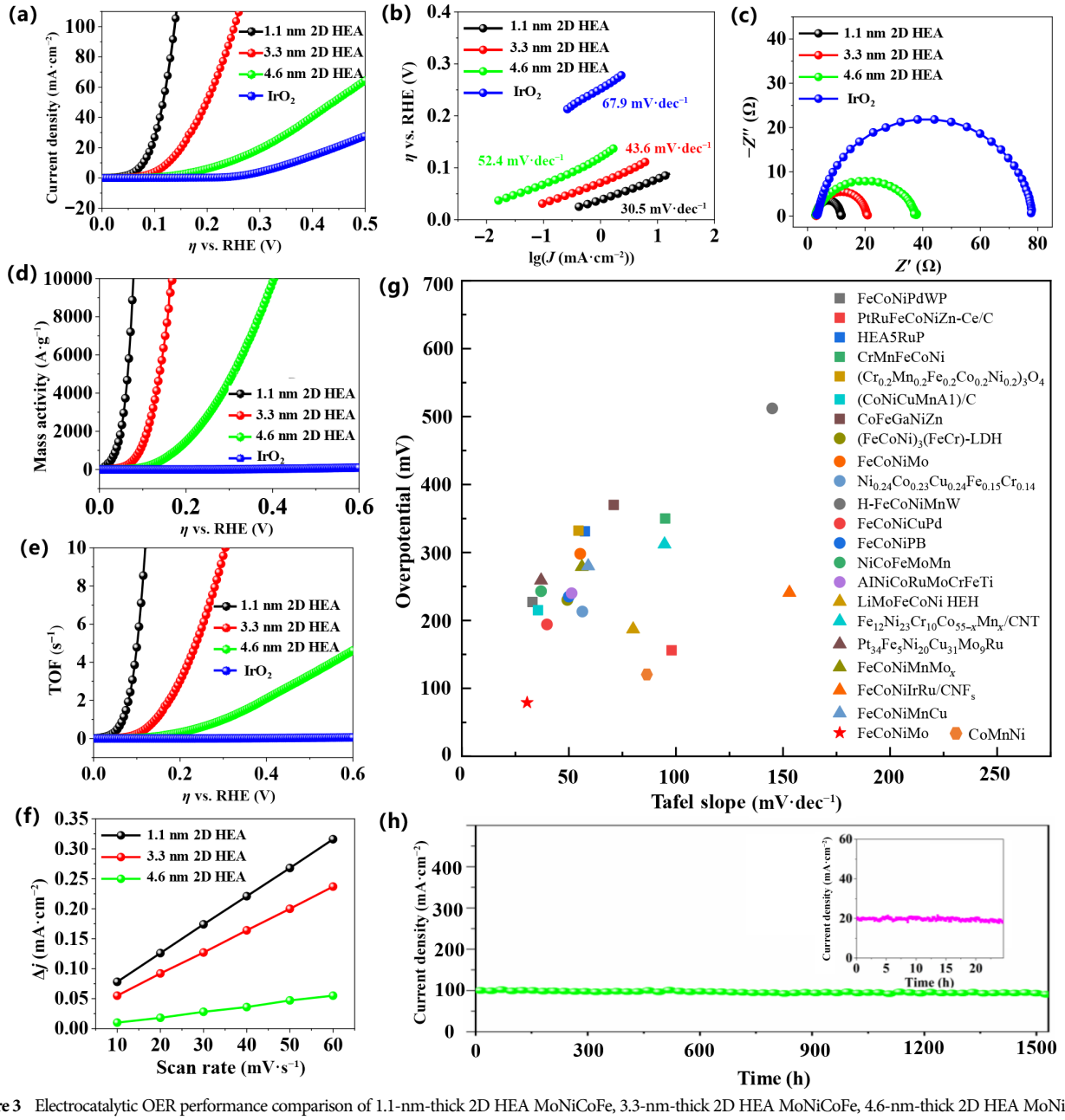

Figure 3 Electrocatalytic OER performance comparison of 1.1-nm-thick 2D HEA MoNiCoFe, 3.3-nm-thick 2D HEA MoNiCoFe, 4.6-nm-thick 2D HEA MoNiCoFe and commercial IrO_2 powders. (a) OER polarization curves; (b) Tafel plots; (c) Nyquist plots; (d) Mass activity determined from current density as a function of η; (e) TOF determined from j as a function of η; (f) Half current density differences ($\Delta j/2$) plots against scan rates; (g) OER performance comparison of 1.1-nm-thick 2D HEA MoNiCoFe and recently reported electrocatalysts; (h) Time-dependent current density curves of 1.1-nm-thick 2D HEA MoNiCoFe, and commercial IrO_2 powders (inset).

benchmark catalysts (343 mV) by 264 mV at equivalent current density. This superior performance establishes a new activity paradigm among non-precious OER electrocatalysts and underscores the critical advantage of atomic-level thickness in 2D HEA electrocatalysts.

Tafel analysis was systematically conducted to evaluate the electrocatalytic kinetics of ultrathin 2D HEA FeCoNiMo across varying thicknesses, with benchmark comparisons to commercial IrO_2. As depicted in Fig. 3(b), the 1.1 nm 2D HEA exhibited a remarkably low Tafel slope of 30.5 mV·dec^{-1}, significantly lower than thicker counterparts (43.6 mV·dec^{-1} for 3.3 nm; 52.4 mV·dec^{-1} for 4.6 nm). This exceptional kinetic parameter substantially outperformed the benchmark IrO_2 catalyst (67.9 mV·dec^{-1}) by 37.4 mV·dec^{-1}. The observed inverse correlation between nanofilm thickness and Tafel slope indicates exponentially enhanced charge transfer kinetics at atomic-scale dimensions.

Electrochemical impedance spectroscopy (EIS) was employed to quantify charge-transfer resistance (R_{ct}) and elucidate its contribution to the enhanced OER kinetics in ultrathin 2D HEA FeCoNiMo. Nyquist plots (Fig. 3(c)) revealed a substantially diminished semicircular arc for the 1.1 nm HEA compared to thicker analogues. Quantitative analysis yielded a remarkably low R_{ct} value of 8.2 Ω for the ultrathin 1.1 nm variant, approximately 2.1-fold and 3.9-fold lower than 3.3 nm (17.5 Ω) and 4.6 nm (32.3 Ω) counterparts, respectively. This low R_{ct} (8.2 Ω) also represented a 9.1-fold reduction relative to the commercial IrO_2 benchmark (74.6 Ω). The precipitous decrease in R_{ct} was primarily attributed to geometrically minimized charge-transfer pathways

resulting from atomic-level ultrasmall thickness [35, 36]. Such dimensional reduction facilitates near-barrierless electron tunneling between catalytic active sites and conductive substrate, effectively approaching the kinetic overpotential limit for proton-coupled electron transfer.

The atomic-level thickness in ultrathin 2D architectures fundamentally maximizes electrochemically active site density. As quantified in Fig. 3(d), the 1.1 nm 2D HEA FeCoNiMo delivered an exceptional mass activity of 9725.2 $A \cdot g^{-1}$ at η = 79 mV, exceeding thicker analogues by 19.3 times (3.3 nm: 502.5 $A \cdot g^{-1}$) and 227.3 times (4.6 nm: 42.8 $A \cdot g^{-1}$). This represents a 1706-fold enhancement over commercial IrO_2 (5.7 $A \cdot g^{-1}$) at equivalent overpotential. When the overpotential was increased to 300 mV, the mass activity of 1.1 nm 2D HEA catalyst reached as high as 1,120,000 $A \cdot g^{-1}$, which is approximately 131,764 times that of commercial IrO_2 (8.5 $A \cdot g^{-1}$) measured under identical conditions. Such extraordinary activity metrics underscore the structural superiority of atomic-thin geometries, where minimized mass loading synergizes with near-unity active site accessibility. These collective advantages position ultrathin 2D HEAs as technologically relevant catalysts for industrial-scale electrolysis systems.

Turnover frequency (TOF), quantifying oxygen molecules generated per active metal site per second, serves as a fundamental metric for intrinsic OER activity. As shown in Fig. 3(e), the ultrathin (1.1 nm) 2D HEA FeCoNiMo achieved a remarkable TOF of 1.94 s^{-1} at η = 79 mV, representing 22.0-fold, 215.6-fold, and 1141.2-fold enhancements over its 3.3 nm (0.088 s^{-1}) counterpart, 4.6 nm (0.009 s^{-1}) counterpart, and commercial IrO_2 (0.0017 s^{-1}), respectively. This exceptional catalytic efficiency stems from ultrathin 2D morphological advantages. The concurrent maximization of mass activity and TOF validated that the ultrathin 2D HEA could minimize critical metal consumption while deliver premium OER performance.

Electrochemical surface areas (ECSAs) were quantitatively evaluated through electric double-layer capacitance (C_{dl}) measurements derived from cyclic voltammetry (Fig. S9 in the ESM). As established in Fig. 3(f), ultrathin 1.1 nm 2D HEA FeCoNiMo demonstrated superior C_{dl} (4.76 $mF \cdot cm^{-2}$), exceeding 3.3 nm (3.64 $mF \cdot cm^{-2}$) and 4.6 nm (0.91 $mF \cdot cm^{-2}$) counterparts by 30.8% and 423.1%, respectively. This pronounced capacitance enhancement signified a substantial increase in electrochemically accessible active sites upon ultrathin thickness reduction. Atomic-scale confinement further facilitated surface electron density modulation, yielding optimized adsorption energetics critical for electrocatalytic processes. Moreover, the ECSA-normalized LSV curves were presented in Fig. S10 in the ESM to reflect the intrinsic activity of the 2D HEA electrocatalysts. Consistent with the geometric-area-normalized polarization curves (Fig. 3(a)), the ECSA-normalized LSV curves also demonstrated the superior catalytic performance of 1.1 nm 2D HEA and, more importantly, reveal the same trend that reducing the film thickness from 3.3 nm to 1.1 nm led to a significant enhancement in activity. This consistency confirmed that the thickness-dependent activity originated from the intrinsic electronic modulation of the ultrathin 2D morphology rather than from roughness artifacts, and highlights the advantage of the ultrahigh specific surface area of the 2D HEA for efficient OER electrocatalysis.

To benchmark the catalytic superiority of ultrathin 2D HEA FeCoNiMo oxygen evolution catalysts, we conducted a comparative analysis of overpotential at 10 $mA \cdot cm^{-2}$ and Tafel slope against state-of-art high-entropy systems as well as representative ternary multi-principal-element systems [37–56]. As evidenced in Fig. 4(g), the 1.1 nm 2D HEA occupies the bottom-left corner, demonstrating simultaneously the lowest overpotential and most favorable Tafel kinetics among all evaluated catalysts. This dual-parameter dominance establishes unprecedented catalytic efficiency relative to nanostructured HEA analogues, including particulate architectures and alternative morphological configurations.

The ultrathin 2D HEA FeCoNiMo demonstrated exceptional electrochemical stability under operating conditions. As evidenced by chronoamperometric analysis (Fig. 4(h)), the 1.1 nm 2D HEA catalyst retained 90% of its initial current density after 1532 hours of continuous OER operation at 100 $mA \cdot cm^{-2}$. This stability was corroborated by minimal activity decay in post-stability polarization curves (Fig. S11 in the ESM) and the absence of noticeable morphological changes after the stability test (Fig. S12 in the ESM). In stark contrast, commercial IrO_2 suffered 10% current loss after merely 24 hours at 10 $mA \cdot cm^{-2}$. Such unprecedented durability, exceeding IrO_2 by a 63.8-fold lifetime enhancement, might be attributed to the high-entropy stability effect within the ultrathin 2D nanostructure. High-entropy-induced electronic structure modulation could suppress metal dissolution, while atomic-scale confinement preventing lattice distortion and phase segregation. The post-OER characterization using XPS and HRTEM were also performed on the ultrathin 2D HEA FeCoNiMo after long-term stability testing. Both XPS (Fig. S13 in the ESM) and HRTEM (Fig. S14 in the ESM) results consistently demonstrated that ultrathin 2D HEA retained metallic without significant reconstruction into oxyhydroxides or other oxidized phases. While HRTEM image further confirmed the retained single-crystalline structure without observable phase segregation, amorphous/poly-crystalline layers, nanoparticle formation. XPS quantification analysis (Table S2 in the ESM) revealed that the Mn/Fe/Co/Ni molar ratios of the 2D HEA remained nearly identical before and after the stability test, implying that no significant dissolution of the metal species occurred during the stability test. These results further verified excellent chemical and structural stability of ultrathin 2D HEA MoNiCoFe in long-time OER operation. This surprising stability was attributed to several factors. First, the ILE synthesis yielded a continuous, atomic-scale-thick nanosheet with a highly uniform elemental distribution, minimizing compositional segregation that typically drives reconstruction. Second, the high configurational entropy combined with the ultrathin geometry may reduce the thermodynamic driving force for phase separation and oxide formation, as the system achieved a kinetically stabilized metallic state. Third, the strong structural integrity of the 2D metallic framework enabled efficient electron transfer while maintaining the pristine alloy surface, obviating the need for reconstruction-induced activation. Therefore, the catalytic activity was primarily attributed to the metallic surface sites, where the high configurational entropy and ultrathin 2D geometry suppress reconstruction.

3.5 DFT calculations

DFT calculations elucidated the enhanced intrinsic OER activity of ultrathin 1.1 nm 2D HEA FeCoNiMo. HRTEM image (Fig. 1(g)) and corresponding SAED pattern (Fig. 1(f)) consistently demonstrate that the ultrathin 2D HEA is single-crystalline and predominantly exposes the (110) facet, as evidenced by the lattice fringes with an interplanar spacing of 0.22 nm corresponding to the (110) plane when viewed along the [110] zone axis. Consistent

with TEM analysis, the predominant (110) facet was modeled to investigate OER thermodynamics via the four-electron pathway (Fig. 4(a)). Gibbs free energy landscapes were computed for eight distinct active sites (Site 1–Site 8, Fig. S15 in the ESM), tracking intermediates *OH→*O→*OOH→O_2 formation energetics [31, 57], where * stands for active sites in the exposed (110) facet. The rate-determining step (rds) was identified as the maximum ΔG in the reaction coordinate [58]. For the Co sites (Site 2 and Site 5), Ni sites (Site 1) and Mo (Site 6 and Site 8) of 2D HEA FeCoNiMo, the ΔG in step 3 (ΔG_3) was larger than those of step 1, step 2 and step 4. While the ΔG in step 4 (ΔG_4) for Fe sites (Site 3, Site 4 and Site 7) of 2D HEA FeCoNiMo was larger than those of step 1, step 2 and step 3. Furthermore, Fe sites at Site 3 presented the smallest ΔG_4 value (1.35 eV) among all the Fe, Co, Ni and Mo sites (Sites 1–8), indicating the formation of O_2 from *OOH in step 4 served as rate-determining step for 2D HEA FeCoNiMo. Importantly, all the ΔG_4 for Fe sites (1.35 eV for Site 3, 1.39 eV for Site 4 and 1.48 eV for Site 7) was lower than the values for Co (1.65 eV for Site 2 and 1.53 eV for Site 5), Ni (1.71 eV for Site 1) and Mo (1.75 eV for Site 6 and 1.62 eV for Site 8), suggesting that Fe atoms acted as the optimal active center aligns with XPS-derived charge redistribution evidence. As a comparison, the Gibbs free energy of thicker 3.3 nm 2D HEA FeCoNiMo was also calculated based on the four-step OER mechanism (Fig. S16 in the ESM). With the thickness increasing to 3.3 nm, the formation of O_2 from *OOH in step 4 still served as rate-determining step for 2D HEA FeCoNiMo, as Fe sites at Site 3 also presented the smallest ΔG_4 value (1.57 eV) among all the metal sites (Fig. 4(b)). Furthermore, the ΔG_4 value (1.35 eV) for Fe sites in the 1.1 nm 2D HEA FeCoNiMo was much lower than ΔG_4 value for Fe sites in the thicker 3.3 nm 2D HEA. This result indicated that the reduction of thickness of ultrathin 2D HEA nanostructure optimized the rate-limiting step, which contributed to the significantly reduced OER overpotential of 2D HEA FeCoNiMo compared to thicker 2D HEA. The enhanced OER activity observed for the 1.1 nm slab may arise predominantly from surface under-coordination and modified electronic states near the surface, rather than from quantum confinement.

DFT calculations further probed the electronic structure origins of enhanced catalytic properties in ultrathin 1.1 nm 2D HEA FeCoNiMo. The total density of states (TDOS, Fig. 4(c)) revealed metallic character of 2D HEA FeCoNiMo with zero bandgap, evidenced by Fermi-level intersection of valence and conduction bands. This computational prediction of high electrical conductivity was consistent with experimental EIS measurements showing minimal charge-transfer resistance. Projected density of

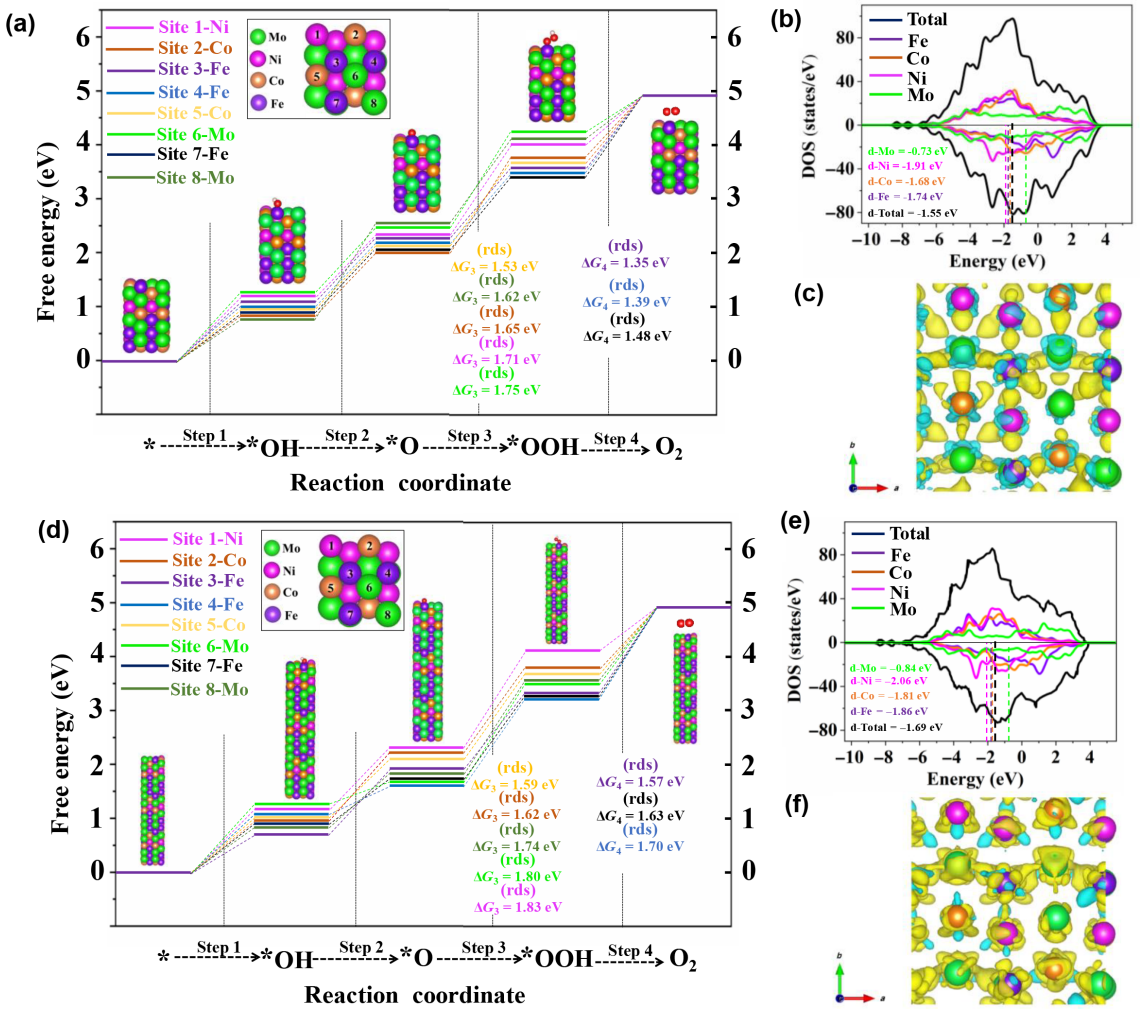

Figure 4 DFT calculation. Gibbs free energy diagram for the four steps of OER on surface active sites 1-8 in (a) 1.1-nm-thick 2D HEA FeCoNiMo and (b) 3.3-nm-thick 2D HEA FeCoNiMo, DOS curves of (c) 1.1-nm-thick 2D HEA FeCoNiMo and (d) 3.3-nm-thick 2D HEA FeCoNiMo. (e) and (f) Charge density difference between 1.1-nm-thick and 3.3-nm-thick 2D HEA FeCoNiMo at different viewing angles. Iso-surface level is 0.012 eV·Å^{-3}. Yellow and blue represent electrons accumulation and depletion, respectively.

states (PDOS) analysis quantified d-band center positions for surface metal sites-a key descriptor of adsorbate binding strength [52]. As shown in Figs. 4(c) and 4(d), d-band center values for Fe, Co, Ni, and Mo sites exhibited significant positive shifts relative to thicker 3.3 nm counterparts. This systematic upshift indicates strengthened catalyst-adsorbate interactions at atomic-scale dimensions. The differential charge density plots in Figs. 4(e) and 4(f) represented differences between the 1.1 nm and 3.3 nm 2D HEA FeCoNiMo slabs. These comparative plots provided useful qualitative insights into thickness-induced electronic modulation, as the yellow regions reflect electron density variations upon reducing slab thickness. The thickness-dependent electronic modulation in our 2D HEA is reflected not only by the DFT-calculated density of states, but also experimentally corroborated by the XPS binding energy shifts (Figs. 2(a)–2(d)), which reveal a charge redistribution from Co/Ni/Mo to Fe upon reducing the slab thickness. The resultant enhanced electron density at Fe active sites facilitates optimized orbital overlap with OER intermediates, thermodynamically manifested through reduced reaction barriers. In the ultrathin 2D HEA, the unique electronic modulation induced by thickness reduction may weaken the *OOH-*OH scaling via altered adsorption geometries and ensemble effects, and the exceptionally low experimental overpotential likely originated from synergistic entropy-stabilized surface effects and thickness-induced electronic modulation beyond the conventional scaling relations.

4 Conclusion

In summary, we demonstrate a facile solution-phase ILE approach for synthesizing ultrathin 2D HEA FeCoNiMo at mild temperatures (80 °C). Atomic-scale confinement to 1.1 nm thickness unlocks exceptional OER performance, achieving ultralow overpotential (η = 79 mV@10 mA·cm^{-2}), favorable Tafel kinetics (30.5 mV·dec^{-1}) and minimal charge-transfer resistance (8.2 Ω). The 1.1 nm 2D HEA delivered exceptional mass activity (9725.2 A·g^{-1}) and turnover frequency (1.94 s^{-1}) at η = 79 mV. This mass activity represented 3 orders of magnitude enhancement over commercial IrO_2 (5.7 A·g^{-1}) at equivalent overpotential, establishing unprecedented efficiency among non-precious OER catalysts. The 2D HEA maintained 90% current retention after 1532 hours of continuous operation at 100 mA·cm^{-2}. This unprecedented durability may attribute to high-entropy stabilization within atomically confined 2D architectures. DFT calculations analysis revealed that thickness reduction optimized rate-determining step energetics and facilitated charge redistribution toward Fe active sites, as well as enhanced intermediates-active sites interaction, thus improving the OER catalytic activity. This work establishes ultrathin 2D HEA as a materials design paradigm for maximizing atom efficiency while minimizing critical metal usage. The synergistic integration of entropy stabilization and atomic-level 2D nanostructure positions these ultrathin 2D HEA as technologically viable catalysts for sustainable energy conversion systems.

Acknowledgements

This work is supported by the National Natural Science Foundation of China (52401031), the Talent Fund of Beijing Jiaotong University (2024XKRC064) and National Training Program of Innovation and Entrepreneurship for Undergraduates (202610004021).

Declaration of conflicting interests

The authors declare no conflicting interests regarding the content of this article.

Data availability

All data needed to support the conclusions in the paper are presented in the manuscript and/or the Supplementary Materials. Additional data related to this paper may be requested from the corresponding author upon request.

Electronic Supplementary Material Supplementary material (further details of the characterizations, electrochemical tests, and DFT calculated structure models, etc.) is available in the online version of this article at https://doi.org/10.26599/NRE.2026.9120246.

References

[1] Zhao, J.; Guo, Y.; Zhang, Z. Q.; Zhang, X. L.; Ji, Q. Q.; Zhang, H.; Song, Z. Q.; Liu, D. Q.; Zeng, J. R.; Chuang, C. H. et al. Out-of-plane coordination of iridium single atoms with organic molecules and cobalt-iron hydroxides to boost oxygen evolution reaction. *Nat. Nanotechnol.* **2025**, *20*, 57–66.

[2] Feng, W. T.; Chang, B.; Ren, Y. F.; Kong, D. B.; Tao, H. B.; Zhi, L. J.; Khan, M. A.; Aleisa, R.; Rueping, M.; Zhang, H. B. Proton exchange membrane water splitting: Advances in electrode structure and mass-charge transport optimization. *Adv. Mater.* **2025**, *37*, 2416012.

[3] Hojjati-Najafabadi, A.; Heidari, G.; Afsharpour, M.; Belver, C.; Aminabhavi, T. M.; Vasseghian, Y.; He, Y. Z. Dual-functional hierarchical NiFe hydroxylphosphate electrocatalyst on copper dendrites for hydrogen and oxygen evolution. *Chem. Eng. J.* **2025**, *518*, 164622.

[4] Anitha, G.; Priyadarshini, R.; Titus, A.; Sahoo, S.; Muppala, C.; Ramkumar, G.; Pham, Q. A.; Rubavathy, S. J.; Rajasimman, M.; Hojjati-Najafabadi, A. Deep learning for the encounter of inorganic nanomaterial for efficient photochemical hydrogen production. *Int. J. Hydrogen Energy* **2024**, *52*, 664–673.

[5] Li, Y.; Chen, G.; Fei, L. S.; Zhou, W.; Shao, Z. P. Designing better electrocatalysts via ion exchange for water splitting. *Adv. Funct. Mater.* **2025**, *35*, 2417880.

[6] Zhang, N. N.; Zhang, Z. L.; Yan, S. W.; Zhang, R.; Yin, P. F.; Du, X. W.; Liu, H. Bridge-oxygen bond: An active group for energy electrocatalysis. *Adv. Funct. Mater.* **2025**, *35*, 2500351.

[7] Shen, Y.; Zhang, X. L.; Qu, M. R.; Ma, J.; Zhu, S.; Min, Y. L.; Gao, M. R.; Yu, S. H. Cr dopant mediates hydroxyl spillover on RuO_2 for high-efficiency proton exchange membrane electrolysis. *Nat. Commun.* **2024**, *15*, 7861.

[8] Zou, X. X.; Zhao, X. Y.; Pang, B. H.; Ma, H.; Zeng, K.; Zhi, S. S.; Guo, H. Interstitial oxygen acts as electronic buffer stabilizing high-entropy alloys for trifunctional electrocatalysis. *Adv. Mater.* **2024**, *36*, 2412954.

[9] Ren, J. T.; Chen, L.; Wang, H. Y.; Yuan, Z. Y. High-entropy alloys in electrocatalysis: From fundamentals to applications. *Chem. Soc. Rev.* **2023**, *52*, 8319–8373.

[10] Wu, J. Z.; He, Y. Z.; Behmadi, R.; Hojati, N.; Xu, L.; Li, C. Y.; Vasseghian, Y.; Hojjati-Najafabadi, A. High-performance self-supporting FeCoNiCrMo HEA catalyst for alkaline hydrogen evolution. *J. Power Sources* **2026**, *669*, 239383.

[11] He, Y. Z.; Tan, R. R.; Li, L. F.; Behmadi, R.; Sun, S. Y.; Zhu, C. S.; Davar, F.; Hojjati-Najafabadi, A. Electrospinning-derived FeCrNiZrMn high-entropy alloy on carbon nanofibers for hydrogen evolution. *ChemCatChem* **2026**, *18*, e01811.

[12] Hojjati-Najafabadi, A.; Behmadi, R.; He, Y. Z.; Kamyab, H.; Vasseghian, Y. Tailoring high-entropy alloys for cutting-edge

hydrogen evolution electrocatalysis. *Sustainable Mater. Technol.* **2025**, *46*, e01655.
[13] Chandran, M. A.; Dutta, P.; Singh, P.; Singh, A. K.; Prasad, B. L.V. Design and synthesis of PtPdNiCoMn high-entropy alloy electrocatalyst for enhanced alkaline hydrogen evolution reaction: A theoretically supported predictive design approach. *Adv. Funct. Mater.* **2025**, *35*, 2418644.
[14] Chandran, M. A.; Sahoo, S.; Singh, A. K.; Prasad, B. L. V. Synthesis framework for designing PtPdCoNiMn high-entropy alloy: A stable electrocatalyst for enhanced alkaline hydrogen evolution reaction. *Small* **2025**, *21*, 2408317.
[15] Chandran, M. A.; Karumuthil, S. C.; Singh, A. K.; Prasad, B. L. V. Electrodeposited Co–Mn–Sn multicomponent alloy as an efficient electrocatalyst for hydrogen evolution reaction. *Int. J. Hydrogen Energy* **2024**, *49*, 658–667.
[16] Mei, Y. J.; Feng, Y. B.; Zhang, C. X.; Zhang, Y.; Qi, Q. L.; Hu, J. High-entropy alloy with Mo-coordination as efficient electrocatalyst for oxygen evolution reaction. *ACS Catal.* **2022**, *12*, 10808–10817.
[17] Hao, J. C.; Zhuang, Z. C.; Cao, K. C.; Gao, G. H.; Wang, C.; Lai, F. L.; Lu, S. L.; Ma, P. M.; Dong, W. F.; Liu, T. X. et al. Unraveling the electronegativity-dominated intermediate adsorption on high-entropy alloy electrocatalysts. *Nat. Commun.* **2022**, *13*, 2662.
[18] Mei, Y. J.; Chen, J. L.; Wang, Q.; Guo, Y. Q.; Liu, H. W.; Shi, W. H.; Lin, C.; Yuan, Y. F.; Wang, Y. H.; Xia, B. Y. et al. MoZn-based high entropy alloy catalysts enabled dual activation and stabilization in alkaline oxygen evolution. *Sci. Adv.* **2024**, *10*, eadq6758.
[19] Tao, L.; Sun, M. Z.; Zhou, Y.; Luo, M. C.; Lv, F.; Li, M. G.; Zhang, Q. H.; Gu, L.; Huang, B. L.; Guo, S. J. A general synthetic method for high-entropy alloy subnanometer ribbons. *J. Am. Chem. Soc.* **2022**, *144*, 10582–10590.
[20] Zhang, M.; Wang, Z. F.; Bo, X.; Huang, R.; Deng, D. H. Two-dimensional catalysts: From model to reality. *Angew. Chem., Int. Ed.* **2025**, *64*, e202419661.
[21] Guo, X. Y.; Zhang, S. L.; Kou, L. Z.; Yam, C. Y.; Frauenheim, T.; Chen, Z. F.; Huang, S. P. Data-driven pursuit of electrochemically stable 2D materials with basal plane activity toward oxygen electrocatalysis. *Energy Environ. Sci.* **2023**, *16*, 5003–5018.
[22] Ying, Y. R.; Fan, K.; Lin, Z. Z.; Huang, H. T. Facing the "cutting edge:" Edge site engineering on 2D materials for electrocatalysis and photocatalysis. *Adv. Mater.* **2025**, *37*, 2418757.
[23] Wang, Y. Z.; Zhang, Z. Y.; Mao, Y. C.; Wang, X. D. Two-dimensional nonlayered materials for electrocatalysis. *Energy Environ. Sci.* **2020**, *13*, 3993–4016.
[24] Lu, D.; Fu, X. Y.; Guo, D.; Ma, W.; Sun, S. H.; Shao, G. L.; Zhou, Z. Challenges and opportunities in 2D high-entropy alloy electrocatalysts for sustainable energy conversion. *SusMat.* **2023**, *3*, 730–748.
[25] Ge, H. Y.; Zheng, L. R.; Yuan, G. B.; Shi, W. X.; Liu, J. L.; Zhang, Y.; Wang, X. Polyoxometallate cluster induced high-entropy oxide sub-1 nm nanosheets as photoelectrocatalysts for Zn-air batteries. *J. Am. Chem. Soc.* **2024**, *146*, 10735–10744.
[26] Sun, Y. F.; Dai, S. Synthesis of high-entropy materials. *Nat. Synth.* **2024**, *3*, 1457–1470.
[27] Wang, F.; Seo, J. H.; Luo, G. F.; Starr, M. B.; Li, Z. D.; Geng, D. L.; Yin, X.; Wang, S. Y.; Fraser, D. G.; Morgan, D. et al. Nanometre-thick single-crystalline nanosheets grown at the water-air interface. *Nat. Commun.* **2016**, *7*, 10444.
[28] Yin, X.; Chen, Q. Y.; Tian, P.; Zhang, P.; Zhang, Z. Y.; Voyles, P. M.; Wang, X. D. Ionic layer epitaxy of nanometer-thick palladium nanosheets with enhanced electrocatalytic properties. *Chem. Mater.* **2018**, *30*, 3308–3314.
[29] Zhang, Z. Y.; Carlos, C.; Wang, Y. Z.; Dong, Y. T.; Yin, X.; German, L.; Berg, K. J.; Bu, W.; Wang, X. D. Nucleation kinetics and structure evolution of quasi-two dimensional ZnO at the air-water interface: An *in situ* time resolved grazing incidence X-ray scattering study. *Nano Lett.* **2022**, *22*, 3040–3046.
[30] Zhao, Y. H.; Wang, Y. Z.; Dong, Y. T.; Carlos, C.; Li, J.; Zhang, Z. Y.; Li, T.; Shao, Y.; Yan, S.; Gu, L. et al. Quasi-two-dimensional earth-abundant bimetallic electrocatalysts for oxygen evolution reactions. *ACS Energy Lett.* **2021**, *6*, 3367–3375.
[31] Yan, G. Y.; Wang, T. L.; Zhao, B. W.; Gao, W. J.; Wu, T.; Ou, L. M. Ultrathin two-dimensional medium-entropy oxide as a highly efficient and stable electrocatalyst for oxygen evolution reaction. *Nano Res.* **2024**, *17*, 2555–2562.
[32] Li, Y. L.; Yan, H. X.; Wang, S. Q.; Luo, X. L.; Kurpaska, Ł.; Fang, F.; Jiang, J. Q.; Kim, H. S.; Huo, W. Y. Toward predictable phase structures in high-entropy oxides: A strategy for screening multicomponent compositions. *Mater. Des.* **2024**, *248*, 113497.
[33] Liu, Y. H.; Hsieh, C. J.; Hsu, L. C.; Lin, K. H.; Hsiao, Y. C.; Chi, C. C.; Lin, J. T.; Chang, C. W.; Lin, S. C.; Wu, C. Y. et al. Toward controllable and predictable synthesis of high-entropy alloy nanocrystals. *Sci. Adv.* **2023**, *9*, eadf9931.
[34] Zhu, H.; Zhu, Z. F.; Hao, J. C.; Sun, S. H.; Lu, S. L.; Wang, C.; Ma, P. M.; Dong, W. F.; Du, M. L. High-entropy alloy stabilized active Ir for highly efficient acidic oxygen evolution. *Chem. Eng. J.* **2022**, *431*, 133251.
[35] Shifa, T. A.; Wang, F. M.; Liu, Y.; He, J. Heterostructures based on 2D materials: A versatile platform for efficient catalysis. *Adv. Mater.* **2019**, *31*, 1804828.
[36] Yan, G. Y.; Wang, Y. Z.; Zhang, Z. Y.; Dong, Y. T.; Wang, J. Y.; Carlos, C.; Zhang, P.; Cao, Z. Q.; Mao, Y. C.; Wang, X. D. Nanoparticle-decorated ultrathin La_2O_3 nanosheets as an efficient electrocatalysis for oxygen evolution reactions. *Nano-Micro Lett.* **2020**, *12*, 49.
[37] He, R.; Wang, S. Q.; Yang, L. L.; Horta, S.; Ding, Y.; Di, C.; Zhang, X. S.; Xu, Y.; Ibáñez, M.; Zhou, Y. T. et al. Active site switching on high entropy phosphides as bifunctional oxygen electrocatalysts for rechargeable/robust Zn-air battery. *Energy Environ. Sci.* **2024**, *17*, 7193–7208.
[38] Jiang, Y.; Liang, Z.; Liu, J. C.; Fu, H.; Yan, C. H.; Du, Y. P. Stimulating electron delocalization of lanthanide elements through high-entropy confinement to promote electrocatalytic water splitting. *ACS Nano* **2024**, *18*, 19137–19149.
[39] Cai, Z. X.; Bolar, S.; Ito, Y.; Fujita, T. Enhancing oxygen evolution reactions in nanoporous high-entropy catalysts using boron and phosphorus additives. *Nanoscale* **2024**, *16*, 4803–4810.
[40] Raj, G.; Nandan, R.; Kumar, K.; Gorle, D. B.; Mallya, A. B.; Osman, S. M.; Na, J.; Yamauchi, Y.; Nanda, K. K. High entropy alloying strategy for accomplishing quintuple-nanoparticles grafted carbon towards exceptional high-performance overall seawater splitting. *Mater. Horiz.* **2023**, *10*, 5032–5044.
[41] Wu, H.; Zhang, J. F.; Lu, Q.; Li, Y. J.; Jiang, R.; Liu, Y.; Zheng, X. R.; Zhao, N. Q.; Li, J. J.; Deng, Y. D. et al. High-entropy layered double hydroxides with highly adjustable components for enhancing electrocatalytic oxygen evolution. *ACS Appl. Mater. Interfaces* **2023**, *15*, 38423–38432.
[42] Cao, X. H.; Gao, Y. T.; Wang, Z. H.; Zeng, H. Z.; Song, Y. F.; Tang, S. G.; Luo, L. X.; Gong, S. FeNiCrCoMn high-entropy alloy nanoparticles loaded on carbon nanotubes as bifunctional oxygen catalysts for rechargeable zinc-air batteries. *ACS Appl. Mater. Interfaces* **2023**, *15*, 32365–32375.
[43] Chen, Z. Q.; Wen, J. B.; Wang, C. H.; Kang, X. W. Convex cube-shaped $Pt_{34}Fe_5Ni_{20}Cu_{31}Mo_9Ru$ high entropy alloy catalysts toward high-performance multifunctional electrocatalysis. *Small* **2022**, *18*, 2204255.
[44] Li, P.; Wan, X. H.; Su, J. H.; Liu, W.; Guo, Y. Z.; Yin, H. Y.; Wang, D. H. Single-phase FeCoNiMnMo high-entropy alloy oxygen evolution anode working in alkaline solution for over 1000 h. *ACS Catal.* **2022**, *12*, 11667–11674.
[45] Hegde, C.; Lim, C. H. J.; Teng, T. H.; Liu, D. B.; Kim, Y. J.; Yan, Q. Y.; Li, H. *In situ* synthesis and microfabrication of high entropy alloy and oxide compounds by femtosecond laser direct writing under ambient conditions. *Small* **2022**, *18*, 2203126.
[46] Chang, S. Q.; Cheng, C. C.; Cheng, P. Y.; Huang, C. L.; Lu, S. Y. Pulse electrodeposited FeCoNiMnW high entropy alloys as efficient and stable bifunctional electrocatalysts for acidic water splitting.

Chem. Eng. J. **2022**, *446*, 137452.
[47] Wang, S. Q.; Xu, B. L.; Huo, W. Y.; Feng, H. C.; Zhou, X. F.; Fang, F.; Xie, Z. H.; Shang, J. K.; Jiang, J. Q. Efficient FeCoNiCuPd thin-film electrocatalyst for alkaline oxygen and hydrogen evolution reactions. *Appl. Catal. B: Environ.* **2022**, *313*, 121472.
[48] Wang, Q. Q.; Li, J. Q.; Li, Y. J.; Shao, G. M.; Jia, Z.; Shen, B. L. Non-noble metal-based amorphous high-entropy oxides as efficient and reliable electrocatalysts for oxygen evolution reaction. *Nano Res.* **2022**, *15*, 8751–8759.
[49] Liu, H.; Qin, H. Y.; Kang, J. L.; Ma, L. Y.; Chen, G. X.; Huang, Q.; Zhang, Z. J.; Liu, E. Z.; Lu, H. M.; Li, J. X. et al. A freestanding nanoporous NiCoFeMoMn high-entropy alloy as an efficient electrocatalyst for rapid water splitting. *Chem. Eng. J.* **2022**, *435*, 134898.
[50] Mwemezi, M.; Prabakar, S. J. R.; Han, S. C.; Park, W. B.; Seo, J. Y.; Sohn, K. S.; Pyo, M. Zinc anodes modified by one-molecular-thick self-assembled monolayers for simultaneous suppression of side-reactions and dendrite-formation in aqueous zinc-ion batteries. *Small* **2022**, *18*, 2201284.
[51] Sun, Z.; Zhao, Y. J.; Sun, C.; Ni, Q.; Wang, C. Z.; Jin, H. B. High entropy spinel-structure oxide for electrochemical application. *Chem. Eng. J.* **2022**, *431*, 133448.
[52] Yu, X. W.; Wang, B.; Wang, C.; Zhuang, C.; Yao, Y. F.; Li, Z. S.; Wu, C. P.; Feng, J. Y.; Zou, Z. G. 2D high-entropy hydrotalcites. *Small* **2021**, *17*, 2103412.
[53] Wang, S. Q.; Huo, W. Y.; Fang, F.; Xie, Z. H.; Shang, J. K.; Jiang, J. Q. High entropy alloy/C nanoparticles derived from polymetallic MOF as promising electrocatalysts for alkaline oxygen evolution reaction. *Chem. Eng. J.* **2022**, *429*, 132410.
[54] Sharma, L.; Katiyar, N. K.; Parui, A.; Das, R.; Kumar, R.; Tiwary, C. S.; Singh, A. K.; Halder, A.; Biswas, K. Low-cost high entropy alloy (HEA) for high-efficiency oxygen evolution reaction (OER). *Nano Res.* **2022**, *15*, 4799–4806.
[55] Huang, K.; Peng, D. D.; Yao, Z. X.; Xia, J. Y.; Zhang, B. W.; Liu, H.; Chen, Z. B.; Wu, F.; Wu, J. S.; Huang, Y. Z. Cathodic plasma driven self-assembly of HEAs dendrites by pure single FCC FeCoNiMnCu nanoparticles as high efficient electrocatalysts for OER. *Chem. Eng. J.* **2021**, *425*, 131533.
[56] Chandran, M. A.; Dutta, P.; Singh, A. K.; Prasad, B. L. V. Platinum-free electrocatalysts based on electrodeposited Co–Mn–Ni alloys for efficient electrocatalytic alkaline water splitting. *ACS Appl. Energy Mater.* **2025**, *8*, 11633–11642.
[57] Cui, M. J.; Yang, C. P.; Li, B. Y.; Dong, Q.; Wu, M. L.; Hwang, S.; Xie, H.; Wang, X. Z.; Wang, G. F.; Hu, L. B. High-entropy metal sulfide nanoparticles promise high-performance oxygen evolution reaction. *Adv. Energy Mater.* **2021**, *11*, 2002887.
[58] Zhang, X.; Yan, F.; Ma, X. Z.; Zhu, C. L.; Wang, Y.; Xie, Y.; Chou, S. L.; Huang, Y. J.; Chen, Y. J. Regulation of morphology and electronic structure of FeCoNi layered double hydroxides for highly active and stable water oxidization catalysts. *Adv. Energy Mater.* **2021**, *11*, 2102141.

Guangyuan Yan received his PhD degree from the Department of Materials Science and Engineering at Dalian University of Technology. During his doctoral studies, he was also a joint-training graduate student at University of Wisconsin-Madison in the United States. He is currently a lecturer and master's supervisor in the school of mechanical, electronic and control engineering at Beijing Jiaotong University. His major research focuses on high-entropy alloys, nano-energy materials, as well as materials intelligent design and forming. He received grants from National Natural Science Foundation of China and the Natural Science Foundation of Beijing Municipality.

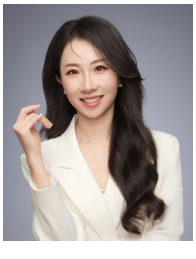

Yunhe Zhao received her PhD degree from School of Materials Science and Chemical Engineering at Harbin Engineering University. During her doctoral studies, she was also a joint-training graduate student at the University of Wisconsin-Madison in the United States. She is currently an associate professor and doctoral supervisor in the College of Chemistry, Chemical Engineering and Resource Utilization, Northeast Forestry University. Her major research focuses on nanoscience and clean energy technologies. She received grants from National Natural Science Foundation of China and the China Postdoctoral Science Foundation.

Wenbo Yu received his PhD degree from Université de Poitiers-French Academy of Sciences at the French from 2010 to 2014. He was a postdoctoral researcher in Department of Materials Science and Engineering at Tsinghua University from 2015 to 2017. He is currently a full professor and doctoral supervisor in the school of mechanical, electronic and control engineering at Beijing Jiaotong University. His research interests include advanced metal materials and forming manufacturing technology. In 2025, Professor Yu was honored as a recipient of the National Young Talent Program.